

# Petrography and geochemistry of a newly discovered Martian gabbroic shergottite NWA 16254

Jun-Feng CHEN (✉), Xinyi TIAN, Fengke CAO

Research Center for Planetary Science, College of Earth and Planetary Sciences,  
Chengdu University of Technology, Chengdu 610059, China

© The Author(s) 2025. Published by Higher Education Press. This is an open access article under the CC BY license (<http://creativecommons.org/licenses/by/4.0>)

**Abstract** The Martian meteorite North-west Africa (NWA) 16254 is classified as a gabbroic shergottite, representing the first documented geochemically depleted member of this textural group. This coarse-grained cumulate comprises pyroxenes (augite and pigeonite), maskelynite, and accessory phases, exhibiting a two-stage crystallization history: 1) early high-pressure formation of Mg-rich pyroxene cores (4.3–9.3 kbar) at the Martian mantle–crust transition zone, followed by 2) shallow crustal crystallization (< 4 kbar) of Fe-enriched pyroxene rims and plagioclase. Geochemical analyses reveal a depleted shergottite signature characterized by pronounced light rare earth element (LREE) depletion and redox conditions indicative of a reduced mantle source. The oxygen fugacity ( $fO_2$ ) calculated via pigeonite-core Eu oxybarometry yields  $\log fO_2 = -1.0 \pm 0.2$ , corroborated by late-stage  $Ti^{3+}$ -bearing ilmenite assemblages, which reflect sustained reducing conditions during crystallization. The bulk-rock major element compositions and Mg# values closely align with the depleted shergottite Queen Alexandra Range (QUE) 94201, suggesting a potential cognate origin from a shared magma system. The gabbroic texture and protracted crystallization history of NWA 16254 provide critical insights into prolonged magma chamber evolution within the Martian crust, implicating episodic melt extraction from a long-lived, incompatible element-depleted mantle reservoir. These findings redefine textural diversity among depleted shergottites and underscore the need for geochronological studies to resolve temporal links between ancient mantle processes and Amazonian magmatism.

**Keywords** shergottite, gabbroic, Mars, oxygen fugacity, fayalite

Received March 17, 2025; accepted March 28, 2025

E-mail: [JFeng.chen@outlook.com](mailto:JFeng.chen@outlook.com)

## 1 Introduction

Martian meteorites represent the only direct samples available in laboratory for studying the composition and evolution of the Martian mantle, as most are igneous in origin and retain geochemical fingerprints of mantle processes. Among these available samples, shergottites, comprising ~90% of the Martian meteorite collection, are particularly critical for deciphering mantle dynamics, crust-mantle interactions, and magmatic differentiation on Mars (e.g., [McSween et al., 1996](#); [Filiberto et al., 2014](#); [Udry et al., 2020](#)). Shergottites are classified into four petrological subtypes depending on their distinct textural and mineralogical characteristics: including basaltic, olivine-phyric, poikilitic, and gabbroic ([Goodrich, 2002](#); [Bridges and Warren, 2006](#); [Filiberto et al., 2014](#)). These variations reflect distinct formation environments, ranging from shallow subsurface crystallization to potential surface eruptions, with gabbroic shergottites notably preserving coarse-grained textures indicative of slow cooling in crustal magma chambers ([Filiberto et al., 2014, 2018](#); [Udry et al., 2020](#)).

Gabbroic shergottites, characterized by cumulate pyroxene and maskelynite, provide unique insights into late-stage magmatic processes and crustal assimilation. Their chemical compositions, while broadly basaltic, reveal evidence of crystal accumulation and prolonged fractional crystallization, offering critical constraints on redox conditions and crustal interactions ([Filiberto et al., 2014, 2018](#)). Recent discoveries of abundant coarse-grained fayalite grains in Martian impact craters highlight the significance of such lithologies in reconstructing magmatic histories and shock metamorphism, as their origins remain poorly understood ([Schmidt et al., 2025](#)). These textures and geochemical heterogeneities make gabbroic shergottites key archives for probing subsurface magmatism and crustal evolution.

Here, we present a comprehensive mineralogical and

geochemical investigation of the newly identified gabbroic shergottite NWA 16254. We aim to 1) characterize its primary mineral assemblages and shock metamorphism features, 2) classify its petrogenetic lineage within the shergottite suite, and 3) reconstruct its crystallization history to elucidate magma chamber dynamics and crustal contamination processes. By integrating textural observations with in situ geochemical analyses, this work advances our understanding of Martian magmatic systems and refines existing models for shergottite formation.

---

## 2 Methods

### 2.1 TIMA analyses

Mineralogical and chemical analyses of the NWA 16254 sample were performed via the TESCAN Integrated Mineral Analyzer (TIMA). The TIMA system is equipped with a scanning electron microscope (SEM) and four energy-dispersive X-ray spectroscopy (EDS) detectors, and the analyses were conducted at the State Key Laboratory of Ore Deposit Geochemistry (SKLOGD), Institute of Geochemistry, Chinese Academy of Sciences (IGCAS). The sample was prepared by embedding it in epoxy resin and polishing it to a mirror finish to ensure optimal imaging quality. Data were collected via the dot mapping technique, with the sample scanned pixel by pixel to generate detailed compositional maps. A pixel size of 1  $\mu\text{m}$  was used to achieve high spatial resolution in the chemical analysis. The SEM instrument was operated at an accelerating voltage of 25 kV, with a probe current of 8.14 nA. Bulk-rock compositional estimates were derived by integrating electron probe microanalysis (EPMA)-determined mineral chemistry with their respective modal abundances.

### 2.2 Major element analyses

The major element compositions of the minerals were determined via a JXA 8230 electron probe microanalyzer (EPMA) at SKLOGD, IGCAS. The nominal analytical conditions for the silicates and oxide minerals were a 25 kV accelerating voltage and a 10 nA beam current. A focused electron beam with a 10  $\mu\text{m}$  defocused beam was used to analyze the mineral compositions. The peak counting times were 30 s for Mn, Ni, Cr, V, and Ti and 10 s for Fe, Na, Si, Mg, Al, K, P and Ca. A set of natural minerals and synthetic glasses were used as standards. Calibration was performed via well-characterized natural and synthetic mineral standards, and matrix corrections were applied via the ZAF (Z-atomic number, A-absorption, F-fluorescence) correction procedure. The counting time for each element was set to 20 s for the

peak and 10 s for the background. The detection limit for major elements was typically < 0.03 wt.% for all the elements.

### 2.3 Trace element analyses

In situ trace element analysis of the mineral phases within the slab was performed via laser ablation-inductively coupled plasma-mass spectrometry (LA-ICP-MS) at Nanjing FocuMS Technology Co. Ltd. The analytical setup combined a Teledyne Cetac Technologies Analyte Excite laser ablation system (Bozeman, MT, USA) with an Agilent Technologies 7700x quadrupole ICP-MS (Hachioji, Japan). A 193 nm ArF excimer laser, homogenized via an optical beam delivery system, was directed onto mineral surfaces at a fluence of 4.5 J/cm<sup>2</sup>. Each analytical cycle comprised a 20-s gas blank acquisition (background signal) followed by 45 s of ablation using a 33  $\mu\text{m}$  laser spot diameter at a repetition rate of 5 Hz. Helium, which flows at 370 mL/min, serves as the primary carrier gas to transport ablated particles from the cell, with subsequent mixing of argon (~1.15 L/min) through a T-junction prior to introduction into the ICP source.

For calibration, USGS basaltic reference glasses (BHVO-2G, BCR-2G, ARM-1, and ARM-2) were selected as external standards because of their anhydrous silicate matrix compatibility. Offline data processing was performed using the ICPMSDataCal software (Liu et al., 2008), which employs a 100% normalization protocol without internal standardization. To ensure analytical reliability, Chinese Geological Standard Glasses QC KL-2 (prepared by the National Research Center for Geoanalysis, Beijing, China) were analyzed as quality control materials. The relative standard deviations of all the QC KL-2 samples were less than 10% for all the elements analyzed.

The trace element composition of the bulk rock was analyzed via an inductively coupled plasma-mass spectrometer (PE DRC-e) at SKLOGD, IGCAS. Fifty milligrams of rock powder was digested with a mixture of hydrofluoric acid and nitric acid (HF + HNO<sub>3</sub>) in high-pressure Teflon bombs at 185°C for two days. Rh standard solutions were used for internal calibration, and international standards OU-6, AGV-2, and GBPG-1 were used as reference materials to monitor analytical quality. The relative standard deviation of the reproducibility for most trace elements was below 10%.

---

## 3 Results

### 3.1 Petrography and mineral chemistry

The mineral modal abundances of NWA 16254 examined

in this study were calculated via TIMA mapping. The results indicate that this sample consists of 46.6 vol.% augite, 23.3 vol.% maskelynite, 14.8 vol.% pigeonite, 5.7 vol.% olivine, 3.9 vol.% quartz, 3.5 vol.% Fe–Ti oxides, and ~2.1 vol.% phosphate. Sample NWA 16254 in this study exhibits distinct cumulate textures of pyroxene and maskelynite (Fig. 1).

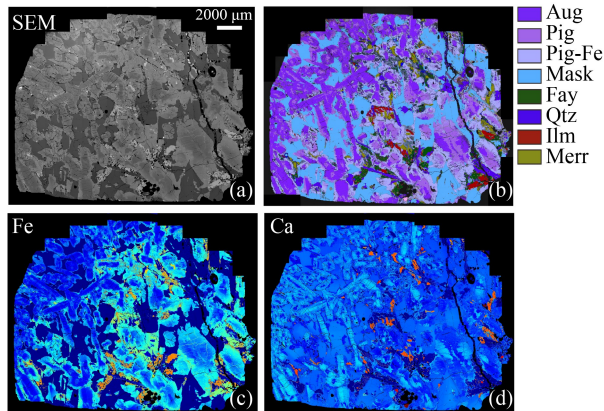


**Fig. 1** Image of the entire NWA 16254 sample studied in this work. (a) A backscattered electron (BSE) image obtained by TIMA. (b) Mineralogical mapping via TIMA. (c) Distribution map of the iron content obtained via TIMA. (d) Distribution map of the calcium content obtained via TIMA.

Aug = augite, Pig = pigeonite, Pig-Fe = Fe-rich pigeonite; Mask = maskelynite, Fay = fayalite, Qtz = quartz; Ilm = ilmenite.

### 3.1.1 Pyroxene

The pyroxene in NWA 16254 is predominantly coarse-grained (up to 400  $\mu\text{m}$ ) and ranges from subhedral to anhedral in crystal shape, exhibiting distinct zoning patterns across three textural domains: core, mantle, and rim (Figs. 1 and 2). The representative major and rare earth element (REE) compositions are shown in Table 1. The cores primarily consist of augite, with a compositional range of  $\text{Wo}_{33-39}\text{En}_{36-40}\text{Fs}_{25-28}$  (average  $\text{Wo}_{36}\text{En}_{39}\text{Fs}_{26}$ ), and minor pigeonite, with a range of  $\text{Wo}_{11-18}\text{En}_{25-47}\text{Fs}_{37-57}$  (average  $\text{Wo}_{15}\text{En}_{36}\text{Fs}_{48}$ ). The mantles are composed of augite and pigeonite, with compositions ranging from  $\text{Wo}_{32}\text{En}_{36}\text{Fs}_{32}$  to  $\text{Wo}_{18}\text{En}_{14}\text{Fs}_{68}$ . The rims almost consist of Fe-enriched pigeonite, which is compositional discontinuous and extremely Fe-rich ( $\text{Wo}_{14}\text{En}_4\text{Fs}_{82}$ ), which is commonly reported in Martian and lunar meteorites (e.g., Warren et al., 2004; Joy et al., 2008; Udry et al., 2017). The  $\text{Al}_2\text{O}_3$  content decreases progressively from cores (1.57 wt.%) to mantles (0.97 wt.%) and further to rims (0.71 wt.%). The Ti/Al ratios in pyroxene cores (in both pigeonite and augite) are relatively low ( $0.13 \pm 0.06$ ) but increase gradually to values up to ~0.70 in Fe-rich rims, correlating with decreasing Mg# (Figs. 3(b), 3(c)).

While major elements (e.g., Ca and Mg) exhibit pronounced zoning (Figs. 2(c), 2(d)), both the cores and

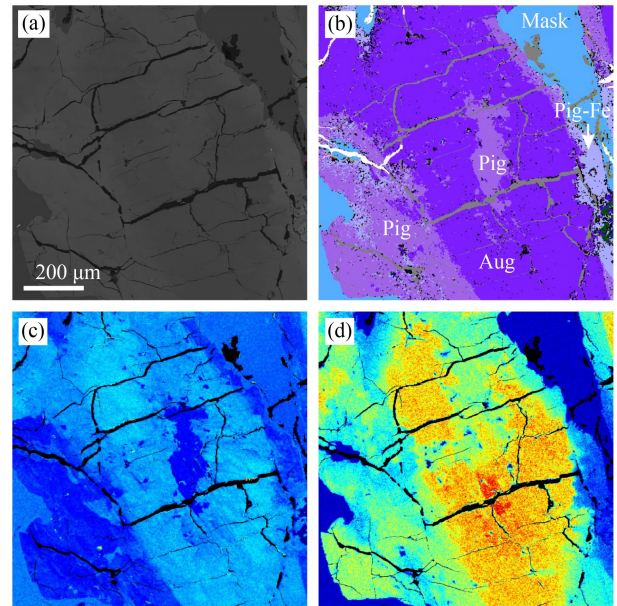


**Fig. 2** Image of the representative pyroxene in the NWA 16254 sample. (a) A backscattered electron (BSE) image obtained by TIMA. (b) Mineralogical mapping by TIMA. (c) Distribution map of the calcium content obtained by TIMA. (d) Distribution map of the magnesium elemental content obtained by TIMA.

Aug = augite, Pig = pigeonite, Mask = maskelynite, Pig-Fe = Fe-rich pigeonite.

rims of the pyroxene grains exhibit similar rare earth element (REE) distribution patterns, although there are notable variations in REE concentrations (Fig. 4(a)). Additionally, the core to mantle to rim homogeneity of REE distribution patterns in individual pyroxene grains (Fig. 4(b)) demonstrates decoupled geochemical behavior, maintaining primordial REE signatures despite a systematic Mg# zonation (from 59 to 39 and then to 16). Notably, both the Mg-rich cores and Fe-enriched rims show significant Eu depletion, with  $\text{Eu}/\text{Eu}^*$  ( $\text{Eu}_{\text{CI}}/[\text{Sm}_{\text{CI}} \times \text{Gd}_{\text{CI}}]^{1/2}$ ) values of  $0.33 \pm 0.11$  ( $n = 20$ , 1SD) in the cores and  $0.34 \pm 0.15$  ( $n = 25$ , 1SD) in the rims.

### 3.1.2 Maskelynite

Maskelynite in NWA 16254 exhibits subhedral to anhedral shapes, with grain sizes reaching up to  $4 \times 2$  mm. Major element compositions are restricted to a relatively narrow range ( $\text{Ab}_{34-57}$ ,  $\text{An}_{40-66}$ ,  $\text{Or}_{0-3}$ ; average  $\text{Ab}_{44}\text{An}_{55}\text{Or}_1$ ; Table 1). Compared to the gabbroic shergottites NWA 7320 ( $\text{Ab}_{45}\text{An}_{52}\text{Or}_3$ ; Udry et al., 2017), our samples of plagioclase have lower  $\text{K}_2\text{O}$  content. The REE distribution patterns of maskelynite exhibit relatively uniform LREE compositions with pronounced positive Eu anomalies (Fig. 3(c)).

### 3.1.3 Phosphates

In NWA 16254, merrillite is the predominant phosphate

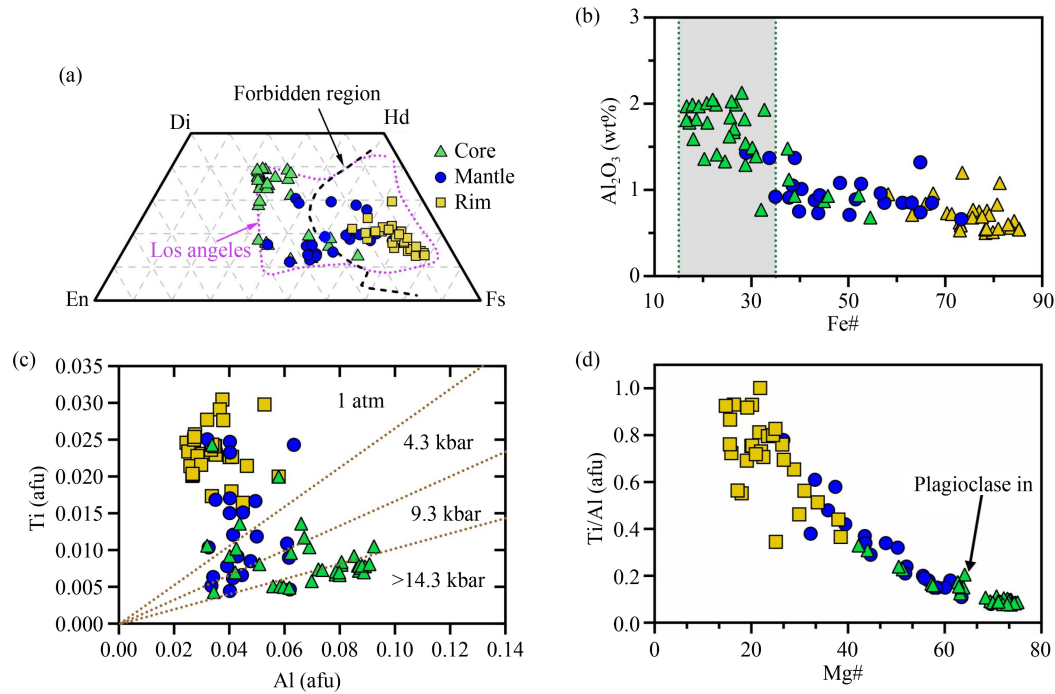


**Fig. 3** Plots of pyroxene compositions analysis in the NWA 16254. (a) Pyroxene quadrilateral for NWA 16254 pyroxenes, including the purple dashed field representing the compositional range of Los Angeles pyroxenes (Warren et al., 2004). The black dashed line represents the pyroxene “forbidden region”, which indicates a zone where pyroxene is unstable (Lindsley, 1983). (b) Pyroxene Fe# versus  $\text{Al}_2\text{O}_3$  content. The  $\text{Fe}\# < 35$  in pyroxene does not have a negative correlation with the  $\text{Al}_2\text{O}_3$  content, indicating that the core crystallization of pyroxene was not influenced by plagioclase interference. (c) Pyroxene Al versus Ti with experimental fields for crystallization pressure from Filiberto et al. (2010). (d) Pyroxene Mg# versus the Ti/Al ratio shows increase Ti/Al with decreasing Mg#.

**Table 1** Major and trace element compositions of representative pyroxene, maskelynite and phosphate minerals in shergottite NWA 16254.

	QC KL-2				Aug Core	Aug Mantle	Pig Core	Pig Rim	Mask Core	Mask Rim	Ap Core	Merr Core
	Conc.	1 $\sigma$	D.I.	Ref								
<i>wt. %</i>												
SiO <sub>2</sub>	50.5	0.78	0.12	50.3	49.3	46.4	52.5	48.8	54.2	53.8	0.02	< 0.01
TiO <sub>2</sub>	2.59	0.05	< 0.01	2.56	0.51	0.74	0.20	0.77	0.07	0.03	–	–
Al <sub>2</sub> O <sub>3</sub>	13.5	0.26	< 0.01	13.3	0.96	0.51	1.62	0.85	28.8	29.3	0.03	0.03
Cr <sub>2</sub> O <sub>3</sub>	–	–	–	–	0.74	0.06	1.69	0.54	–	0.03	–	–
FeO	10.9	0.2	0.001	10.7	26.4	36.5	11.1	25.3	0.40	0.39	0.89	4.32
MnO	0.16	0	< 0.01	0.17	0.77	0.86	0.37	0.69	0.03	0.01	0.09	0.17
MgO	7.51	0.15	< 0.01	7.34	11.5	5.16	17.5	8.47	0.12	0.12	0.02	1.24
CaO	11.2	0.23	0.04	10.9	8.49	7.50	15.8	13.4	12.6	13.3	53.9	46.8
Na <sub>2</sub> O	2.36	0.04	< 0.01	2.35	0.11	0.00	0.12	0.05	4.04	3.98	0.09	1.01
K <sub>2</sub> O	0.49	0.01	< 0.01	–	< 0.01	< 0.01	0.01	0.02	0.05	0.03	< 0.01	0.04
P <sub>2</sub> O <sub>5</sub>	0.27	0	< 0.01	0.23	–	–	–	–	< 0.01	0.03	41.0	45.5
Cl											1.32	0.01
F											1.46	< 0.01
O = F, Cl											0.91	–
Total	99.4	–	–	97.8	98.7	97.7	100.8	98.9	100.3	101.0	99.8	99.1
Mg#	72.1	–	–	72.2	43.6	20.1	73.7	37.4	35.3	36.0	4.0	33.8
Fs					56.9	74.2	25.0	53.6				
En					24.7	10.5	39.4	18.0				

(continued)

	QC KL-2				Aug Core	Aug Mantle	Pig Core	Pig Rim	Mask Core	Mask Rim	Ap Core	Merr Core
	Conc.	1 $\sigma$	D.I.	Ref								
Wo					18.3	15.3	35.5	28.5				
Ab									36.6	35.1		
An									63.1	64.7		
Or									0.27	0.20		
<i>ppm</i>												
Li	5.80	0.24	0.54	5.10	3.88	1.57	2.27	1.27	4.94	5.32	0.77	2.42
Be	1.30	0.21	0.28	0.88	< 0.01	0.00	0.00	0.00	0.21	0.10	0.02	0.04
B	3.19	0.41	0.98	2.73	1.12	0.29	0.85	0.29	0.08	0.79	5.52	1.16
Sc	30.0	0.59	0.16	31.8	87.9	90.0	99.1	83.9	0.47	0.69	1.13	92.7
V	310	5.72	< 0.01	309	562	124	194	52.1	2.27	2.55	0.72	7.8
Cr	292	5.44	2.59	294	6745	1761	2650	592	2.17	1.31	0.00	32.9
Co	45.1	0.86	0.05	41.2	29.9	41.8	42.5	39.7	0.56	0.46	0.23	2.47
Ni	112	2.22	0.68	112	10.5	4.26	5.03	5.37	0.00	0.20	0.00	0.36
Cu	92.5	1.81	0.46	87.9	1.86	0.22	1.07	0.58	0.00	0.64	0.15	0.50
Zn	114	5.00	0.94	110	22.9	94.3	75.5	133	5.68	5.13	4.24	13.4
Ga	22.5	0.46	0.04	20.0	4.50	5.09	4.62	5.91	38.6	35.8	2.03	4.31
Ge	2.43	0.40	1.61	1.30	1.14	1.23	1.18	2.81	0.55	0.00	0.09	2.85
As	0.00	0.19	0.79	0.17	0.26	0.09	0.24	0.00	0.00	0.00	0.22	1.33
Rb	8.64	0.20	0.06	8.70	< 0.01	< 0.01	0.00	0.04	0.00	0.05	0.04	0.37
Sr	359	6.67	< 0.01	356	9.89	1.16	1.12	1.39	113	108	178	229
Y	24.9	0.52	< 0.01	25.4	5.38	8.31	7.70	11.2	0.09	0.11	92.7	1576
Zr	154	3.12	< 0.01	152	1.15	1.58	1.30	2.73	0.02	0.00	12.0	32.6
Nb	13.9	0.28	< 0.01	15.0	< 0.01	< 0.01	< 0.01	0.00	0.00	0.00	0.01	0.01
Mo	3.69	0.19	0.09	3.60	0.14	0.14	0.14	0.15	0.00	0.00	0.03	0.07
Cd	0.00	0.02	0.24	0.09	0.00	0.00	0.13	0.07	0.00	0.00	0.00	0.05
Sn	1.47	0.09	0.14	1.54	0.09	0.13	0.18	0.10	0.27	0.32	0.23	0.19
Sb	0.25	0.05	0.14	0.14	0.00	0.00	< 0.01	0.05	0.03	0.17	0.01	0.00
Cs	0.12	0.01	0.04	0.12	< 0.01	< 0.01	0.00	< 0.01	0.01	0.01	0.00	0.01
Ba	121	2.73	0.11	123	10.0	0.00	< 0.01	0.09	1.93	1.91	5.84	5.89
La	13.1	0.31	< 0.01	13.1	< 0.01	< 0.01	< 0.01	0.01	0.01	0.02	2.54	46.7
Ce	31.8	0.67	< 0.01	32.4	0.09	0.06	0.06	0.05	0.05	0.03	9.52	147
Pr	4.62	0.12	< 0.01	4.60	< 0.01	0.02	0.02	0.03	0.01	0.00	2.12	29.0
Nd	22.6	0.58	0.06	21.6	0.24	0.25	0.20	0.30	0.02	0.06	14.8	192
Sm	5.57	0.26	< 0.01	5.54	0.19	0.26	0.27	0.32	0.05	0.01	8.28	105
Eu	2.01	0.08	< 0.01	1.92	0.07	0.05	0.03	0.06	0.84	0.80	1.77	17.1
Gd	5.66	0.22	< 0.01	5.92	0.63	0.75	0.67	0.82	0.06	0.04	16.5	209
Tb	0.84	0.04	< 0.01	0.89	0.13	0.18	0.16	0.21	0.00	0.00	2.90	39.8
Dy	5.18	0.18	0.04	5.22	0.95	1.48	1.26	2.02	0.02	0.04	18.6	278
Ho	0.98	0.04	0.01	0.96	0.22	0.34	0.29	0.47	0.00	0.00	3.80	58.9
Er	2.54	0.11	< 0.01	2.54	0.67	1.17	0.98	1.62	0.00	0.03	9.74	162
Tm	0.34	0.02	< 0.01	0.33	0.10	0.19	0.15	0.22	0.00	0.00	1.17	21.0
Yb	2.09	0.11	< 0.01	2.10	0.58	1.28	1.07	1.78	0.00	0.00	6.32	123

(continued)

	QC KL-2				Aug Core	Aug Mantle	Pig Core	Pig Rim	Mask Core	Mask Rim	Ap Core	Merr Core
	Conc.	1 $\sigma$	D.l.	Ref								
Lu	0.28	0.02	< 0.01	0.29	0.09	0.21	0.15	0.28	0.00	0.00	0.82	16.6
Hf	3.90	0.16	< 0.01	3.93	0.06	0.11	0.08	0.16	0.00	0.00	0.10	1.02
Ta	0.89	0.04	< 0.01	0.96	0.00	0.00	0.00	0.00	0.00	0.00	0.00	0.00
W	0.38	0.04	< 0.01	0.37	< 0.01	< 0.01	0.00	0.00	0.01	0.00	0.00	0.50
Pb	2.00	0.09	0.05	2.07	0.03	< 0.01	0.02	< 0.01	0.00	0.02	0.19	0.53
Bi	0.04	0.01	0.04	0.04	0.02	0.03	< 0.01	< 0.01	0.00	0.01	0.00	0.00
Th	1.03	0.04	< 0.01	1.02	< 0.01	0.00	0.00	0.00	0.00	0.00	0.33	2.14
U	0.56	0.03	< 0.01	0.55	< 0.01	0.00	0.00	0.00	0.00	0.00	0.35	0.21

Notes: “-” = data not available; Conc. = concentration in ppm; d.l. = detection limit. Mineral abbreviations: Aug = augite; Pig = pigeonite; Mask = maskelynite; Ap = apatite; Merr = merrillite. The combined standard errors ( $1\sigma$ ), derived from counting statistics, natural concentration variations during ablation, and propagated uncertainties in standard values during each analytical session, were less than 10% for most elements, except Bi, Ge, Be, B, and Sb.

phase, occurring as significantly larger and more abundant grains compared to apatite. Despite their contrasting modal abundances and grain sizes, both minerals exhibit remarkably similar REE patterns. However, they display significant differences in their REE abundances (Fig. 4(d)). Merrillite shows higher chondrite-normalized REE concentrations than other phases in shergottites do, whereas apatite is characterized

by lower overall REE contents (e.g., Shearer et al., 2015; Udry et al., 2017; Orr et al., 2022). Both minerals consistently demonstrate LREE depletion, as evidenced by their chondrite-normalized La/Lu ratios of  $0.29 \pm 0.06$  (merrillite) and  $0.25 \pm 0.05$  (apatite). Notably, apatite exhibits a more pronounced Eu anomaly, with Eu/Eu\* values averaging  $0.69 \pm 0.22$ , in contrast to the weaker anomaly of merrillite ( $\text{Eu}/\text{Eu}^* = 0.37 \pm 0.06$ ) (Table 1).

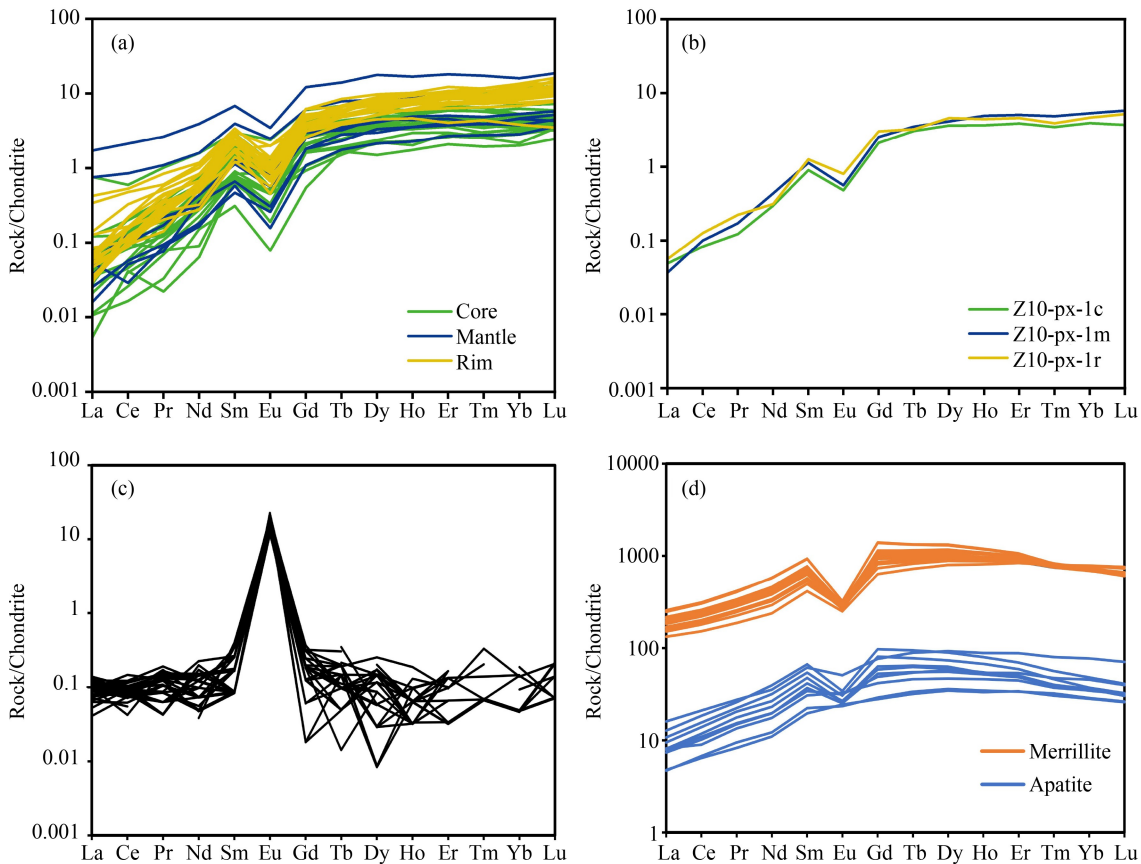


**Fig. 4** Chondrite-normalized REE profiles of NWA 16254 in this study. (a) REE profiles of pyroxene from core to rim. (b) Representative REE profiles of one pyroxene grain from core to rim. (c) and (d) REE profiles of maskelynite and phosphates, respectively.

### 3.1.4 Fe–Ti oxides

Fe-Ti oxides in the studied assemblage are dominated by ilmenite, occurring as discrete grains or intergrown with titanomagnetite and commonly mantled by fayalite rims (Figs. 5(a), 5(b)). Microprobe analyses reveal that ilmenite compositions approach ideal  $\text{FeTiO}_3$  endmember ( $\text{Ilm}_{100}$ ) with minor substitutions of Mn or Cr (Table 2). In contrast, titanomagnetite exhibits compositional variations ranging from  $\text{Usp}_{82}\text{Mt}_{18}$  to  $\text{Usp}_{90}\text{Mt}_{10}$  (where Usp = ulvöspinel and Mt = magnetite).

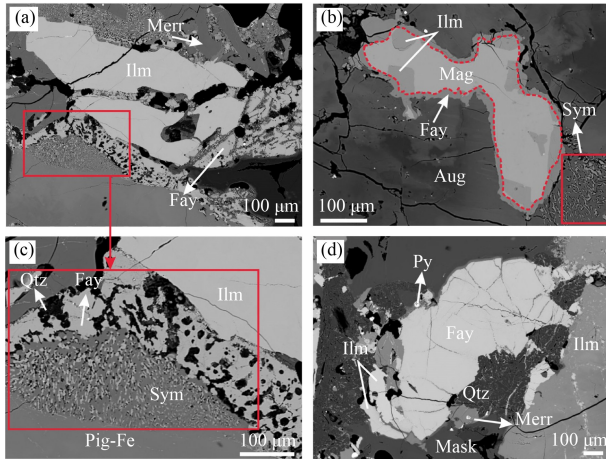


**Fig. 5** Back-scattered electron (BSE) images of NWA 16254. (a) and (b) Representative BSE images of Fe-Ti oxides. (a) Ilmenites are commonly surrounded by merrillite and fayalite. (b) Ilmenite and titanomagnetite exhibit intergrowth textures, and both minerals are predominantly surrounded by rims composed of fayalite. (c) Three-phase symplectite in association with ilmenite, quartz and fayalite. (d) BSE image of representative large fayalite grains (up to 1000  $\mu\text{m}$  in length). Aug = augite, Pig = pigeonite, Pig-Fe = Fe-rich pigeonite; Mask = maskelynite, Fay = fayalite, Qtz = quartz; Ilm = ilmenite; Py = pyrite; Mag = titanomagnetite Sym = symplectite.

### 3.1.5 Symplectite and fayalite

Three-phase symplectites, consisting of Fe-enriched pigeonite, fayalitic olivine, and silica, were identified in NWA 16254 (Figs. 5(a) and 5(c)). Similar assemblages have also been reported in other Martian meteorites, including Los Angeles, QUE 94201, and Shergotty (McSween et al., 1996; Aramovich et al., 2002; Warren et al., 2004; Udry et al., 2017). These symplectites are commonly associated with late-stage minerals such as merrillite and Fe-Ti oxides (ilmenite and titanomagnetite). These symplectitic fayalite grains are predominantly less than 10  $\mu\text{m}$  in size (Figs. 5(a), 5(b) and 5(c)). Notably, some fayalite grains, whose crystal size can reach up to 1000  $\mu\text{m}$ , were also observed in shergottite NWA 16254 (Fig. 5(d)). These fayalite crystals exhibit remarkably consistent Fe# ( $100 \times \text{molar Fe}^{2+}/[\text{Fe}^{2+} + \text{Mg}]$ ) values, with a mean composition of  $93.3 \pm 2.1$  ( $n = 11$ , 1 SD) (Table 2).

### 3.2 Bulk rock major and rare earth element compositions

The bulk-rock major and REE compositions of NWA 16254 are listed in Table 3. The meteorite exhibits a low bulk Mg# ( $100 \times \text{molar Mg}/[\text{Fe}^{2+} + \text{Mg}]$ ) of 37.5, consistent with the basaltic shergottite QUE 94201 (Mg# = 37.6; Lodders, 1998), but lower than most olivine-phyric shergottites. Major element abundances (e.g.,  $\text{Al}_2\text{O}_3$ ,  $\text{Na}_2\text{O}$ ,  $\text{TiO}_2$ , and CaO) of NWA 16254 also align with those of the shergottite QUE 94201 (Lodders, 1998), as shown in Fig. 6. The REE pattern of NWA 16254 is consistent with that of depleted shergottites due to a pronounced light rare earth element (LREE) depletion pattern (Fig. 7). The  $(\text{La}/\text{Yb})_{\text{CI}}$  ratio in this study is 0.18, which is consistent with the geochemical characteristics of depleted shergottites (e.g., Udry et al., 2020). Additionally, the Sr (102 ppm) and Ba (241 ppm) contents are relatively higher than those of most depleted shergottites (Sr < 100 ppm, Ba < 80 ppm, respectively). However, the  $\text{Ce}/\text{Ce}^*$  ( $\text{Ce}_{\text{CI}}/[\text{La}_{\text{CI}} \times \text{Pr}_{\text{CI}}]^{1/2}$ ) value is  $1.03 \pm 0.07$ , which is consistent with most previously identified depleted shergottites, and the average  $\text{Ce}/\text{Ce}^*$  value of depleted shergottites is  $0.96 \pm 0.04$  (data from the compilation by Udry et al. (2020)).

## 4 Discussion

### 4.1 Crystallization sequences and conditions

#### 4.1.1 Crystallization sequences

Sample NWA 16254 can be classified as gabbroic shergottite based on its cumulate texture, which implies prolonged magmatic differentiation. Gabbroic shergottites such as NWA 16254 are linked to basaltic shergottites through magmatic processes (Udry et al., 2020). Therefore, these types of shergottites have similar geochemical compositions and crystallization sequences. Previous experimental studies have demonstrated that low-Ca pyroxene (e.g., pigeonite) is the liquidus phase of basaltic shergottite melts, followed by augite crystallization (Stolper and McSween, 1979). However, in NWA 16254 meteorite, pigeonite and augite cores coexist without significant Mg# divergence (pigeonite: Mg# = 71–74; augite: Mg# = 70–73; Figs. 1(c), 2(d)), indicating both minerals crystallized simultaneously during early-stage cooling. The core-to-rim zoning patterns in pyroxenes, characterized by Mg-rich cores ( $\text{Wo}_{43}\text{En}_{40}\text{Fs}_{17}$ ) and Fe-enriched rims ( $\text{Wo}_{19}\text{En}_{13}\text{Fs}_{69}$ ) (Fig. 1(c)), was commonly discovered in other gabbro shergottites (e.g., NWA 7320; Udry et al., 2017) and basaltic shergottites (e.g., Los Angeles; Warren et al., 2004). Therefore, the Mg-rich cores in pyroxene crystallized earlier than the Fe-enriched rims did.

**Table 2** Major element compositions of representative Fe-Ti oxides and fayalite.

Comment	Ilmenite			Titanomagnetite			Fayalite		
	Ilm3	Ilm5	Ilm7	Mag6	Mag7	Mag9	OI-1	OI-9	OI-6
SiO <sub>2</sub>	0.04	0.00	0.10	0.14	0.06	0.16	30.5	30.2	30.0
TiO <sub>2</sub>	52.9	53.1	53.1	25.1	27.4	25.3	0.08	0.07	0.14
Al <sub>2</sub> O <sub>3</sub>	0.04	0.08	0.03	2.24	2.87	2.94	0.00	0.00	0.00
Cr <sub>2</sub> O <sub>3</sub>	0.08	0.20	0.10	6.48	5.88	6.05	0.03	0.00	0.00
FeO	45.7	45.7	45.8	62.6	60.9	62.4	62.6	65.1	64.1
MnO	0.68	0.64	0.66	0.57	0.60	0.64	1.23	1.26	1.32
MgO	0.33	0.25	0.37	0.24	0.26	0.14	3.62	1.81	2.54
NiO	0.01	0.00	0.00	0.00	0.00	0.03	0.00	0.00	0.00
CaO	–	–	–	–	–	–	0.27	0.76	0.27
P <sub>2</sub> O <sub>5</sub>	–	–	–	–	–	–	0.37	0.16	0.39
Total	99.8	100.0	100.2	97.4	98.0	97.7	98.7	99.4	98.8
Fe#	1.26	0.95	1.42	0.68	0.75	0.41	9.34	4.71	6.58
Cations									
Si	0.00	0.00	0.00	0.01	0.00	0.01	1.02	1.01	1.01
Ti	1.00	1.01	1.00	0.71	0.77	0.71	0.00	0.00	0.00
Al	0.00	0.00	0.00	0.10	0.13	0.13	0.00	0.00	0.00
Cr	0.00	0.00	0.00	0.19	0.17	0.18	0.00	0.00	0.00
Fe <sup>3+</sup>	–0.01	–0.02	–0.02	0.28	0.16	0.26	–0.07	–0.04	–0.06
Fe <sup>2+</sup>	1.01	1.02	1.02	1.68	1.74	1.69	1.82	1.87	1.86
Mn	0.01	0.01	0.01	0.02	0.02	0.02	0.03	0.04	0.04
Mg	0.01	0.01	0.01	0.01	0.01	0.01	0.18	0.09	0.13
Ni	0.00	0.00	0.00	0.00	0.00	0.00	0.00	0.00	0.00
Ca	–	–	–	–	–	–	0.01	0.03	0.01
P	–	–	–	–	–	–	0.01	0.00	0.01
Total	2.00	2.00	2.00	3.00	3.00	3.00	3.00	3.00	3.00
X <sub>Ilm</sub>	1.01	1.02	1.02	–	–	–	–	–	–
X <sub>Usp</sub>	–	–	–	0.83	0.91	0.84	–	–	–

Notes. “–” = data not available.

The negative Fe<sup>3+</sup> values for ilmenite suggest crystallization under reducing conditions.

**Table 3** Bulk-rock compositions of trace elements in NWA 16254.

Comment	International standards			NWA16254 This study	QUE 94201 Lodders (1998)
	OU-6	AGV-2	GBPG-1		
Li	95.1	10.5	20.3	9.03	–
Be	2.57	2.13	0.82	0.07	–
Sc	23.3	12.5	14.5	31.0	48.0
V	134	121	102	70.2	113
Cr	70.7	16.2	174	753	–
Co	30.3	16.1	20.3	19.6	24.0
Ni	41.3	20.7	57.2	7.96	20.0
Cu	40.8	53.3	31.3	6.74	–
Zn	115	90.3	81.5	55.7	110
Ga	25.4	20.1	19.5	24.0	27.0
Ge	5.31	3.79	3.55	7.61	–

(continued)

Comment	International standards			NWA16254 This study	QUE 94201 Lodders (1998)
	OU-6	AGV-2	GBPG-1		
As	14.8	2.75	2.35	0.91	770
Rb	123	68.1	58.6	0.83	–
Sr	135	637	364	102	70.0
Y	27.6	18.9	17.7	21.8	31.0
Zr	183	235	224	34.1	100
Nb	15.6	13.8	10.1	0.72	0.70
Mo	0.98	2.13	1.71	0.30	–
Ag	0.29	0.31	0.26	0.02	–
Cd	0.00	0.04	0.02	–	–
In	0.09	0.05	0.05	0.03	–
Sn	2.79	2.24	2.54	–	–
Sb	0.56	0.45	0.13	–	–
Cs	8.19	1.13	0.32	0.04	–
Ba	499	1091	879	241	15.0
La	34.7	37.1	51.3	0.63	0.40
Ce	76.9	65.9	99.5	1.95	1.00
Pr	8.15	7.65	11.2	0.34	–
Nd	30.4	29.0	41.9	2.27	2.20
Sm	6.09	5.31	6.59	1.29	2.30
Eu	1.43	1.52	1.75	0.76	1.04
Gd	5.54	4.50	4.71	2.52	4.30
Tb	0.89	0.62	0.59	0.52	0.87
Dy	5.24	3.30	3.11	3.84	5.80
Ho	1.06	0.65	0.65	0.85	1.19
Er	2.98	1.73	1.92	2.49	–
Tm	0.46	0.25	0.29	0.38	–
Yb	3.16	1.55	1.94	2.53	3.30
Lu	0.47	0.24	0.29	0.36	0.50
Hf	4.93	4.76	5.64	1.26	3.41
Ta	1.09	0.79	0.37	0.09	0.02
W	1.60	0.68	0.36	0.48	–
Tl	0.53	0.25	0.24	0.01	–
Pb	30.1	13.1	13.2	0.11	–
Bi	0.91	0.37	0.16	0.25	–
Th	11.9	6.09	11.6	–	0.05
U	2.01	1.85	0.87	0.04	0.05

Notes: The relative standard deviations (RSD) of replicate analyses for most trace elements were < 5%, while data for low-concentration elements (Ge, As, Mo, Ag, Cd, In, Sn, Sb, W, Tl, Bi) were considered reference values.

Comparing the Al content with the Fe# content in pyroxene can help constrain the crystallization sequence of pyroxene versus plagioclase (Stolper and McSween, 1979; Mikouchi, 1999; Barrat et al., 2002). A negative correlation between the Al<sub>2</sub>O<sub>3</sub> content and Fe# in pyroxene was observed in shergottite NWA 16254 (Fig.

3(b)), suggesting the start of plagioclase crystallization from the melt. However, the pyroxene core (Fe# < 35) did not show such a negative correlation. This indicates that pyroxene cores crystallized first, followed by Fe-rich pyroxene rims and plagioclase, simultaneously (Wenzel et al., 2021). With the crystallization of pyroxene and

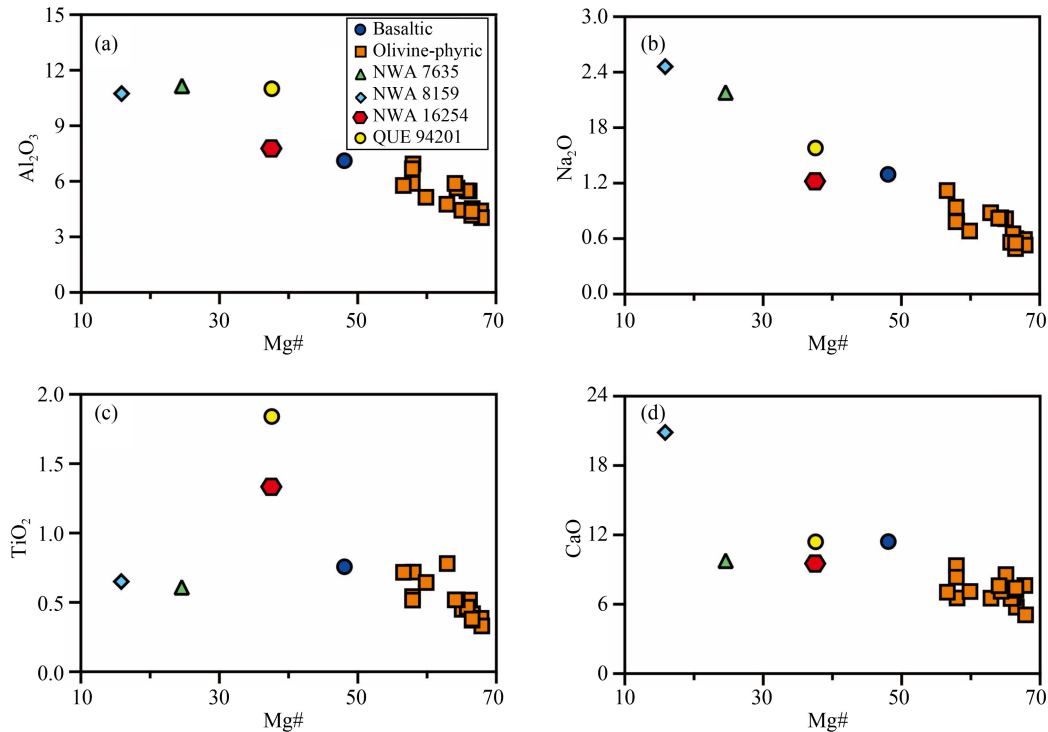


**Fig. 6** Plots comparing the bulk rock compositions of  $\text{Al}_2\text{O}_3$ ,  $\text{Na}_2\text{O}$ ,  $\text{TiO}_2$ , and  $\text{CaO}$  versus  $\text{Mg}\#$  in NWA 16254. The bulk rock major element compositions of NWA 16254 are similar to those of most depleted basaltic shergottites.

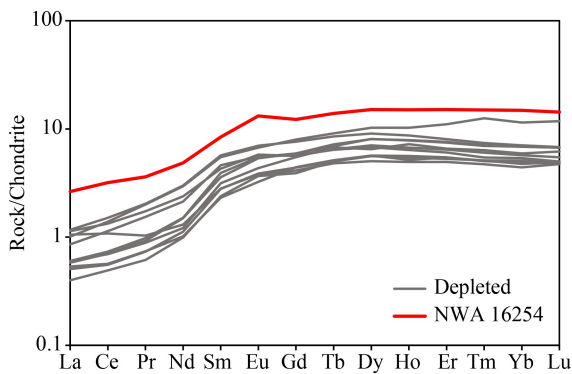


**Fig. 7** Chondrite-normalized rare earth element patterns of whole-rock for NWA 16254 meteorite and other depleted shergottites. The gray lines represent data from Udry et al. (2020).

plagioclase, the residual magma also crystallized some accessory minerals. Textural relationships indicate that phosphates (merrillite, apatite) crystallized first, succeeded by Fe-Ti oxides (ilmenite, titanomagnetite) and sulfides, as the residual melt evolved toward volatile-enriched, late-stage conditions.

#### 4.1.2 Crystallization conditions

The Ti/Al ratios of pyroxene are commonly used to estimate the crystallization pressure of Martian meteorites after the calibration of the crystallization pressure in terrestrial magmatic rocks of by Nekvasil et al. (2004). The Ti/Al ratios of early pyroxene in NWA 16254 are

consistent with crystallization prior to plagioclase at pressures between 4.3 and 9.3 kbar (Fig. 3(c)), corresponding to depths between 30 and 70 km on Mars (Filiberto et al., 2010). The Fe-rich rims of pyroxene exhibit discrete Al and Ti relationships due to the crystallization of plagioclase (Fig. 3(c)), potentially indicating that crystallization occurred at a relatively shallow Martian subsurface. The “forbidden region” in which pyroxene is not stable at low pressure (Lindsley, 1983) results in the decomposition of Fe-enriched pyroxene. This evidence, as shown in Fig. 3(a), supports low-pressure crystallization conditions. Some Fe-rich pyroxene grains reach lengths of up to 5 mm, consistent with prolonged growth under low-pressure, slow-cooling conditions. Considering these pyroxene characteristics, sample NWA 16254 may have also experienced a two-stage crystallization history (Udry et al., 2020).

#### 4.1.3 Oxygen fugacity

Experimental studies have established the crystallization sequence of basaltic shergottites, with low-Ca pyroxene (pigeonite) as the first crystallizing phase (Stolper and McSween, 1979; McKay et al., 1994; Wadhwa et al., 1994; Minitti and Rutherford, 2000; Wadhwa, 2001; McCanta et al., 2004). Consequently, pigeonite preserves the earliest magmatic compositional signatures and redox conditions, with its oxygen fugacity reflecting that of the primitive magma (Chen et al., 2024). In contrast, ilmenite-titanomagnetite assemblages crystallized during

late-stage magmatic evolution. Comparative analysis of  $fO_2$  variations between pyroxene and ilmenite pairs could therefore reconstruct redox evolution throughout the magmatic system.

The remarkably consistent REE patterns and concentrations observed across core-mantle-rim transects of individual pyroxene grains (Fig. 4(b)) demonstrate preservation of their primary geochemical signatures, suggesting these REE distributions remained unaffected by post-crystallization processes such as impact metamorphism or secondary weathering alteration. Although, this sample is a gabbroic shergottite exhibiting cumulate textures, major and trace element compositions of these types of shergottites are consistent with basaltic rocks (Udry et al., 2020), supporting the use of whole-rock data to estimate oxygen fugacity. Furthermore, previous studies have demonstrated that the REE patterns of whole-rock basaltic shergottites are parallel to parent melts (e.g., Lundberg et al., 1988; Wadhwa et al., 1994; Wadhwa, 2001; McSween et al., 1996), indicating that the Eu anomalies in pyroxene can effectively record the oxidation state of the parent magma. Therefore, applying the pyroxene Eu oxybarometer to whole-rock compositions is a valid approach for reconstructing the oxygen fugacity of primitive magmas in both basaltic and gabbroic shergottites (McCanta et al., 2004).

To apply the Eu in pyroxene oxybarometer to NWA 16254, this study selected REE data from the core domains of pigeonite crystals, where the chemical signatures remain unaffected by subsequent plagioclase crystallization, and utilized the bulk rock composition as the parental magma proxy for oxygen fugacity calculation. The oxygen fugacity was constrained through the quantitative relationship between the chondrite-normalized  $(Eu/Sm)_{CI}$  ratio in pyroxene and its corresponding ratio in the primitive melt. For NWA 16254, the measured pyroxene  $(Eu/Sm)_{CI}$  ratio was  $0.45 \pm 0.15$  ( $n = 9$ , 1SD), with a calculated partition coefficient  $D(Eu/Sm)_{pyroxene/melt}$  of  $0.27 \pm 0.09$ . This yielded an estimated oxygen fugacity of IW (iron-wüstite buffer)  $-1.0 \pm 0.2$ , reflecting highly reducing conditions consistent with the majority of depleted shergottites documented in previous compilations (Chen et al., 2024).

The ilmenite-titanomagnetite oxybarometer (Sauerzapf et al., 2008) were also applied to constrain oxygen fugacity during late-stage magma crystallization. However, valid estimates could not be obtained due to the near-endmember composition of ilmenite ( $X_{ilm} = 1$ , Table 2), which implies disequilibrium between ilmenite and titanomagnetite. Notably, the ilmenite and titanomagnetite pairs in our samples appear to attain equilibrium (Fig. 8), as three independent mineral pairs consistently plot on the log (Mg/Mn) equilibrium partitioning line defined by experimental or theoretical constraints (Bacon and Hirschmann, 1988).

The thermodynamic calculations also yielded negative

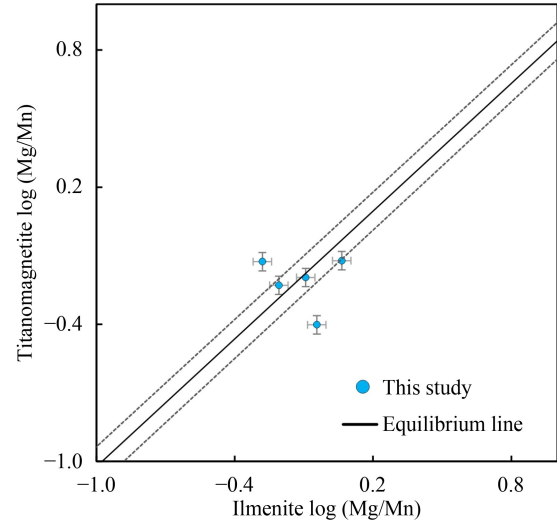


**Fig. 8** Equilibrium test plot for ilmenite-titanomagnetite pairs. The equilibrium line (solid black line) and error envelope (dash black line) from Bacon and Hirschmann 1988.

$Fe^{3+}$  values for ilmenite. This inconsistency indicates a systematic overestimation of the number of cations in the ilmenite formula to maintain charge balance. A plausible resolution involves the substitution of  $Ti^{3+}$  for  $Ti^{4+}$  in the ilmenite structure, as the assumption of exclusively  $Ti^{4+}$  in stoichiometric calculations would artificially inflate the  $Fe^{3+}$  requirements. This interpretation aligns with those of experimental studies demonstrating  $Ti^{3+}$  stabilization under reducing conditions (Sauerzapf et al., 2008), further supporting the relatively reduced redox state.

This late-stage reduction likely supports the stability of the large grain size of fayalite (up to 1000  $\mu m$ ), which occurred in lunar meteorite MIL 05035 (Joy et al., 2008). Previous studies proposed an increase in  $fO_2$  of up to four orders of magnitude during shergottite evolution, attributed to autooxidation and loss of reduced volatiles (e.g., Herd, 2006; Peslier et al., 2010; Grosshans et al., 2013; Castle and Herd, 2017; Howarth and Udry, 2017). However, autooxidation (or crystallization differentiation) can contribute only about one order of magnitude of oxidation, based on experimental simulations by Castle and Herd (2017). Therefore, the NWA 16254 sample likely experiences a limited change in  $fO_2$  during crystallization compared to other shergottites, implying limited degassing. Therefore, this shergottite was likely derived from a previously unsampled Martian reservoir. Further chronological and isotopic analyses are needed to advance the understanding of magmatic system heterogeneity on Mars.

#### 4.2 Geochemical classification of gabbroic NWA 16254

The chondrite-normalized La/Yb ratio has been widely adopted as a robust indicator for characterizing mantle source features in Martian meteorites owing to the relative immobility of REEs during moderate fractional

crystallization (Wadhwa et al., 1994; McSween et al., 1996; Symes et al., 2008). Our analyses of NWA 16254 reveal a pronounced LREE depletion pattern ( $(\text{La}/\text{Yb})_{\text{CI}} = 0.18$ ), which is consistent with the geochemical characteristics of depleted shergottites (Fig. 7). Despite the inherent mobility of Sr and Ba during aqueous alteration, their concentrations (Sr = 102 ppm, Ba = 241 ppm) fall within the range of unaltered shergottites, combined with the absence of positive Ce anomalies ( $\text{Ce}/\text{Ce}^* = 1.03$ ) and preservation of magmatic REE fractionation patterns, collectively suggesting limited terrestrial weathering (Harvey et al., 1993; Wadhwa et al., 1994; Crozaz and Wadhwa, 2001; Borg and Draper, 2003; Crozaz et al., 2003; Wadhwa et al., 1994). Therefore, this NWA 16254 meteorite can be classified as a depleted shergottite on the basis of its geochemical characteristics. Previous studies have identified two gabbroic shergottites: NWA 6963 as an enriched type (Filiberto et al., 2018) and NWA 7320 as an intermediate type (Udry et al., 2017). In contrast, NWA 16254 is the first documented depleted gabbroic shergottite. Its unique two-stage evolutionary history and crystallization sequence offer crucial new constraints for reconstructing magmatic processes in depleted shergottite source regions. Additionally, the Mg#,  $\text{Al}_2\text{O}_3$ ,  $\text{Na}_2\text{O}$ ,  $\text{TiO}_2$ , and CaO contents of NWA 16254 are similar to those of the basaltic shergottite QUE 94201 (depleted geochemical characteristics), as shown in Fig. 5. These findings suggest that these two meteorites may have been derived from the similar magma system.

This geochemical depletion appears to be fundamentally linked to redox conditions during mantle melting. The calculated oxygen fugacity ( $\text{IW} - 1.0 \pm 0.2$ ) aligns with values characteristic of reduced sources (such as the oxygen fugacity for QUE 94201, which is  $-0.6 \pm 0.3$ ) and incompatible element-depleted Martian mantle sources (e.g., Wadhwa, 2001; Herd et al., 2002; McCanta et al., 2004; McCanta et al., 2004; Chen et al., 2024). Critically, Chen et al. (2024) demonstrated that the oxygen fugacities of depleted and intermediate shergottites have likely remained statistically invariant since 2.4 Ga, suggesting long-term stabilization of reduced ( $\text{IW} - 0.38 \pm 0.20$ ) mantle reservoirs. In contrast, enriched shergottites present systematically higher  $f\text{O}_2$  values ( $\text{IW} + 1.12 \pm 0.40$ ; Chen et al., 2024), which are indicative of oxidized mantle sources or late-stage metasomatic overprinting (Herd, 2003; Udry et al., 2020).

The temporal distribution of Martian shergottites reveals fundamental differences in magmatic regimes. Depleted shergottites exhibit an expansive crystallization age range spanning 2.4 billion years (160–2400 Ma) (e.g., Nyquist et al., 2001; Moser et al., 2013; Herd et al.), whereas enriched and intermediate shergottites are confined to a narrow interval of 150–346 Ma (Nyquist et al., 2001; Borg and DePaolo, 2008; Bouvier et al., 2005, 2008). This stark temporal disparity implies that

depleted mantle sources experienced recurrent melt extraction throughout much of Martian history, whereas enriched and intermediate reservoirs were either short-lived or episodically reactivated. As the first documented gabbroic shergottite with unequivocal depleted signatures, NWA 16254 provides a critical opportunity to probe these processes. However, the absence of precise geochronological and radiogenic isotope data (e.g.,  $\epsilon^{143}\text{Nd}$ ,  $\epsilon^{176}\text{Hf}$ , and Pb-Pb isotopes) currently precludes definitive links to specific magmatic episodes. Future studies should prioritize the crystallization age and isotope analyses to assess whether it represents ancient mantle melting (~2.4 Ga) or younger reprocessing and constrain depleted mantle source reservoir evolution.

## 5 Conclusions

NWA 16254 is a gabbroic shergottite characterized by a coarse-grained cumulate texture dominated by pyroxenes (augite and pigeonite), maskelynite, and accessory phases, including phosphate minerals, Fe–Ti oxides, and sulfides. The crystallization sequence began with early-stage Mg-rich pyroxene cores ( $\text{Mg}\# = 65 - 75$ ) forming at 4.3 – 9.3 kbar (30–70 km depth), followed by Fe-enriched pyroxene rims and plagioclase under lower pressures ( $< 4$  kbar), indicating magma ascent and shallow crustal emplacement. Oxygen fugacity remained stable throughout crystallization: early-stage pigeonite cores preserve a reduced signature of  $\text{IW} - 1.0 \pm 0.2$ , whereas late-stage ilmenite-magnetite assemblages lack evidence of oxidation. This suggests either limited degassing or reducing degassing buffered the impact of autoxidation processes. These petrogenetic and redox constraints indicate that NWA 16254 likely originated from a previously unrecognized shergottite terrane, revealing greater diversity in Martian volcanic systems than previously documented.

NWA 16254 is classified as a depleted shergottite based on its pronounced LREE depletion ( $(\text{La}/\text{Yb})_{\text{CI}} = 0.18$ ), low incompatible element abundances (Sr = 102 ppm, Ba = 241 ppm), and mantle-like Ce/Ce\* indicative of minimal terrestrial alteration. This classification aligns with its reduced oxygen fugacity, which is consistent with relatively early melt extraction from a long-lived, incompatible element-depleted Martian mantle reservoir. Owing to their similar bulk-rock compositions and oxygen fugacity, these meteorites may have been derived from the same magma system with QUE 94201. Notably, this newly found NWA 16254 sample is the first gabbroic shergottite exhibiting definitive depleted signatures. Its coarse-grained texture and redox stability may provide critical evidence for prolonged magma chamber evolution in the Martian crust, bridging the gap between rapid basaltic eruptions and plutonic differentiation.

## Acknowledgments

We are very grateful to the Associate Editor Dr. Xiaojia Zeng for handling our manuscript. We greatly appreciate the Associate Editor Dr. Xiaojia Zeng and one anonymous reviewer for their insightful comments and suggestions.

## Supplementary material

**Supplementary material** is available in the online version of this article at <http://doi.org/10.15302/planet.2025.25002> and is accessible for authorized users.

## Data availability

The source data sets supporting the paper have been uploaded to the Science Data Bank with a link <https://doi.org/10.57760/sciencedb.22079>.

## Declaration of competing interests

The authors declare that they have no known competing financial interests or personal relationships that could have appeared to influence the work reported in this paper.

## Author Contributions

**Jun-Feng Chen:** Investigation, Visualization, Writing-Original Draft, Writing-Review & Editing; **Xinyi Tian:** Investigation, Visualization, Writing-Review & Editing; **Fengke Cao:** Writing-Review & Editing.

## References

- Aramovich C J, Herd C D K, Papike J J (2002). Symplectites derived from metastable phases in martian basaltic meteorites. *Am Mineral*, 87: 1351–1359
- Bacon C R, Hirschmann M M (1988). Mg/Mn partitioning as a test for equilibrium between coexisting Fe–Ti oxides. *Am Mineral*, 73(1–2): 57–61
- Borg A M G, DePaolo D (2008). Preliminary age of Martian Meteorite Northwest Africa 4468 and its relationship to the other incompatible-element-enriched shergottites. *Lunar and Planetary Science XXXIX*, abstract #1851.
- Borg L E, Draper D S (2003). A petrogenetic model for the origin and compositional variation of the martian basaltic meteorites. *Meteorit Planet Sci*, 38: 1713–1731
- Bouvier A, Blichert-Toft J, Vervoort J D, Albarède F (2005). The age of SNC meteorites and the antiquity of the Martian surface. *Earth Planet Sci Lett*, 240(2): 221–233
- Bouvier A, Blichert-Toft J, Vervoort J D, Gillet P, Albarède F (2008). The case for old basaltic shergottites. *Earth Planet Sci Lett*, 266(1–2): 105–124
- Bridges J C, Warren P H (2006). The SNC meteorites: basaltic igneous processes on Mars. *J Geol Soc London*, 163(2): 229–251
- Castle N, Herd C D K (2017). Experimental petrology of the Tissint meteorite: Redox estimates, crystallization curves, and evaluation of petrogenetic models. *Meteorit Planet Sci*, 52(1): 125–146
- Chen J F, Zhao Y Y S, Shu Q, Zhou S H, Du W, Yang J (2024). The oxygen fugacity of intermediate shergottite NWA 11043: Implications for Martian mantle evolution. *Geochim Cosmochim Acta*, 375: 90–105
- Crozaz G, Wadhwa M (2001). The terrestrial alteration of Saharan shergottites Dar al Gani 476 and 489: A case study of weathering in a hot desert environment. *Geochim Cosmochim Acta*, 65(6): 971–978
- Crozaz G, Floss C, Wadhwa M (2003). Chemical alteration and REE mobilization in meteorites from hot and cold deserts. *Geochim Cosmochim Acta*, 67(24): 4727–4741
- Filiberto J, Gross J, Trela J, Ferre E C (2014). Gabbroic Shergottite Northwest Africa 6963: An intrusive sample of Mars. *Am Mineral*, 99(4): 601–606
- Filiberto J, Gross J, Udry A, Trela J, Wittmann A, Cannon K M, Penniston-Dorland S, Ash R, Hamilton V E, Meado A L, Carpenter P, Jolliff B, Ferré E C (2018). Shergottite Northwest Africa 6963: A Pyroxene-Cumulate Martian Gabbro. *J Geophys Res Planets*, 123: 1823–1841
- Filiberto J, Musselwhite D S, Gross J, Burgess K, Le L, Treiman A H (2010). Experimental petrology, crystallization history, and parental magma characteristics of olivine-phyric shergottite NWA 1068: Implications for the petrogenesis of “enriched” olivine-phyric shergottites. *Meteorit Planet Sci*, 45: 1258–1270
- Goodrich C A (2002). Olivine-phyric Martian basalts: A new type of shergottite. *Meteorit Planet Sci*, 37: 31–34
- Grosshans T E, Lapen T J, Andreasen R, Irving A J (2013). Lu–Hf and Sm–Nd ages and source compositions for depleted shergottite Tissint. In: 44th Lunar and Planetary Science Conference. University of Houston
- Harvey R P, Wadhwa M, McSween H Y, Crozaz G (1993). Petrography, mineral chemistry, and petrogenesis of antarctic shergottite LEW88516. *Geochim Cosmochim Acta*, 57: 4769–4783
- Herd C D K (2003). The oxygen fugacity of olivine-phyric martian basalts and the components within the mantle and crust of Mars. *Meteorit Planet Sci*, 38(12): 1793–1805
- Herd C D K (2006). Insights into the redox history of the NWA 1068/1110 martian basalt from mineral equilibria and vanadium oxybarometry. *Am Mineral*, 91(10): 1616–1627
- Herd C D K, Borg L E, Jones J H, Papike J J (2002). Oxygen fugacity and geochemical variations in the martian basalts: Implications for martian basalt petrogenesis and the oxidation state of the upper mantle of Mars. *Geochim Cosmochim Acta*, 66(11): 2025–2036
- Herd C D K, Walton E L, Agee C B, Muttik N, Ziegler K, Shearer C K, Bell A S, Santos A R, Burger P V, Simon J I, Tappa M J, McCubbin F M, Gattacceca J, Lagroix F, Sanborn M E, Yin Q Z, Cassata W S, Borg L E, Lindvall R E, Kruijer T S, Brennecka G A, Kleine T, Nishiizumi K, Caffee M W (2017). The Northwest Africa

- 8159 martian meteorite: Expanding the martian sample suite to the early Amazonian. *Geochim Cosmochim Acta*, 218: 1–26
- Howarth G H, Udry A (2017). Trace elements in olivine and the petrogenesis of the intermediate, olivine-phyric shergottite NWA 10170. *Meteorit Planet Sci*, 52(2): 391–409
- Joy K, Crawford I, Anand M, Greenwood R, Franchi I, Russell S (2008). The petrology and geochemistry of Miller Range 05035: A new lunar gabbroic meteorite. *Geochim Cosmochim Acta*, 72: 3822–3844
- Lindsley D H (1983). Pyroxene thermometry. *Am Mineral*, 68: 477–493
- Liu Y S, Hu Z C, Gao S, Gunther D, Xu J, Gao C G, Chen H H (2008). *In situ* analysis of major and trace elements of anhydrous minerals by LA-ICP-MS without applying an internal standard. *Chem Geol*, 257: 34–43
- Lodders K (1998). A survey of shergottite, nakhlite and chassigny meteorites whole-rock compositions. *Meteorit Planet Sci*, 33: A183–A190
- Lundberg L L, Crozaz G, McKay G, Zinner E (1988). Rare earth element carriers in the Shergotty meteorite and implications for its chronology. *Geochim Cosmochim Acta*, 52(8): 2147–2163
- McCanta M C, Rutherford M J, Jones J H (2004). An experimental study of rare earth element partitioning between a shergottite melt and pigeonite: implications for the oxygen fugacity of the martian interior. *Geochim Cosmochim Acta*, 68(8): 1943–1952
- McKay G, Le L, Wagstaff J, Crozaz G (1994). Experimental partitioning of rare-earth elements and strontium: Constraints on petrogenesis and redox conditions during crystallization of Antarctic angrite Lewis Cliff 86010. *Geochim Cosmochim Acta*, 58(13): 2911–2919
- McSween H Y Jr, Eisenhour D D, Taylor L A, Wadhwa M, Crozaz G (1996). QUE94201 shergottite: Crystallization of a Martian basaltic magma. *Geochim Cosmochim Acta*, 60(22): 4563–4569
- Mikouchi (1999) Shocked plagioclase in the lunar meteorites Yamato-793169 and Asuka-881757: Implications for their shock and thermal histories. *Antarc Meteor Res* 12(2): 151–167
- Minitti M E, Rutherford M J (2000). Genesis of the Mars Pathfinder “sulfur-free” rock from SNC parental liquids. *Geochim Cosmochim Acta*, 64(14): 2535–2547
- Moser D E, Chamberlain K R, Tait K T, Schmitt A K, Darling J R, Barker I R, Hyde B C (2013). Solving the Martian meteorite age conundrum using microbaddeleyite and launch-generated zircon. *Nature*, 499(7459): 454–457
- Nekvasil H, Dondolini A, Horn J, Filiberto J, Long H, Lindsley D H (2004). The origin and evolution of silica-saturated alkalic suites: An experimental study. *J Petrol*, 45: 693–721
- Nyquist L E, Bogard D D, Shih C Y, Greshake A, Stöffler D, Eugster O (2001). Ages and Geologic Histories of Martian Meteorites. In: Kallenbach, R. et al., eds. *Chronology and Evolution of Mars*, 96, 105–164.
- Orr K J, Forman L V, Rankenburg K, Evans N J, McDonald B J, Godel B, Benedix G K (2022). Geochemical and mineralogical classification of four new shergottites: NWA 10441, NWA 10818, NWA 11043, and NWA 12335. *Meteorit Planet Sci*, 57(6): 1194–1223
- Peslier A H, Hnatyshin D, Herd C D K, Walton E L, Brandon A D, Lapen T J, Shafer J T (2010). Crystallization, melt inclusion, and redox history of a Martian meteorite: Olivine-phyric shergottite Larkman Nunatak 06319. *Geochim Cosmochim Acta*, 74(15): 4543–4576
- Sauerzapf U, Lattard D, Burchard M, Engelmann R (2008). The titanomagnetite-ilmenite equilibrium: New experimental data and thermo-oxybarometric application to the crystallization of basic to intermediate rocks. *J Petrol*, 49: 1161–1185
- Schmidt M E, Kizovski T V, Liu Y, Hernandez-Montenegro J D, Tice M M, Treiman A H, Hurowitz J A, Klevang D A, Knight A L, Labrie J, Tosca N J, VanBommel S J, Benaroya S, Crumpler L S, Horgan B H N, Morris R V, Simon J I, Udry A, Yanchilina A, Allwood A C, Cable M L, Christian J R, Clark B C, Flannery D T, Heirwegh C M, Henley T L J, Henneke J, Jones M W M, Orenstein B J, Herd C D K, Randazzo N, Shuster D, Wadhwa M (2025). Diverse and highly differentiated lava suite in Jezero crater, Mars: Constraints on intracrustal magmatism revealed by Mars 2020 PIXL. *Sci Adv*, 11: eadr2613
- Shearer C K, Burger P V, Papike J J, McCubbin F M, Bell A S (2015). Crystal chemistry of merrillite from Martian meteorites: Mineralogical recorders of magmatic processes and planetary differentiation. *Meteorit Planet Sci*, 50: 649–673
- Stolper E, McSween H Y (1979). Petrology and origin of the shergottite meteorites. *Geochim Cosmochim Acta*, 43: 1475–1498
- Symes S J K, Borg L E, Shearer C K, Irving A J (2008). The age of the martian meteorite Northwest Africa 1195 and the differentiation history of the shergottites. *Geochim Cosmochim Acta*, 72: 1696–1710
- Udry A, Howarth G H, Herd C D K, Day J M D, Lapen T J, Filiberto J (2020). What Martian Meteorites Reveal About the Interior and Surface of Mars. *J. Geophys. Res. Planets* 125, e2020JE006523.
- Udry A, Howarth G H, Lapen T J, Righter M (2017). Petrogenesis of the NWA 7320 enriched martian gabbroic shergottite: Insight into the martian crust. *Geochim Cosmochim Acta*, 204: 1–18
- Wadhwa M (2001). Redox state of Mars’ upper mantle and crust from Eu anomalies in shergottite pyroxenes. *Science*, 291: 1527–1530
- Wadhwa M, McSween H Y, Crozaz G (1994). Petrogenesis of shergottite meteorites inferred from minor and trace-element microdistributions. *Geochim Cosmochim Acta*, 58: 4213–4229
- Warren P H, Greenwood J P, Rubin A E (2004). Los Angeles: A tale of two stones. *Meteorit Planet Sci*, 39: 137–156
- Wenzel A, Filiberto J, Stephen N, Schwenzer S P, Hammond S J (2021). Constraints on the petrologic history of gabbroic shergottite Northwest Africa 6963 from pyroxene zoning profiles and electron backscattered diffraction. *Meteorit Planet Sci*, 56: 1744–1757